High Porosity in Nanostructured *n*-Type Bi$_2$Te$_3$ Obtaining Ultralow Lattice Thermal Conductivity

Yuan Wang,[1] Wei-Di Liu,[2] Han Gao,[2] Li-Jun Wang,[2] Meng Li,[2] Xiao-Lei Shi,[2] Min Hong,[1]

Hao Wang,[1] Jin Zou,[2,3] and Zhi-Gang Chen*[1,2]

[1]Centre for Future Materials, University of Southern Queensland, Springfield central,

Queensland 4300, Australia.

[2]Materials Engineering, The University of Queensland, Brisbane, Queensland 4072,

Australia. [3]Centre for Microscopy and Microanalysis, The University of Queensland,

Brisbane, Queensland 4072, Australia.

KEYWORDS: *thermoelectrics, bismuth telluride, porous, nanostructure, lattice thermal*

conductivity

ABSTRACT: Porous structure possesses full potentials to develop high-performance thermoelectric materials with low lattice thermal conductivity. In this study, n-type porous nanostructured Bi_2Te_3 pellet is fabricated by sintering Bi_2Te_3 nanoplates synthesized with a facile solvothermal method. With adequate sublimations of Bi_2TeO_5 during the spark plasma sintering, homogeneously distributed pores and dense grain boundaries are successfully introduced into the Bi_2Te_3 matrix, causing strong phonon scatterings. From which, an ultralow lattice thermal conductivity of < 0.1 W m^{-1} K^{-1} is achieved in the porous nanostructured Bi_2Te_3 pellet. With the well-maintained decent electrical performance, a power factor of 10.57 µW cm^{-1} K^{-2} at 420 K, as well as the reduced lattice thermal conductivity secured a promising zT value of 0.97 at 420 K, which is among the highest values reported for pure n-type Bi_2Te_3. This study provides the insight of realizing ultralow

lattice thermal conductivity by synergistic phonon scatterings of pores and nanostructure

in the n-type Bi_2Te_3-based thermoelectric materials.

INTRODUCTION

Thermoelectric materials, enabling the direct solid-state conversion between heat and electricity, are promising to realize emission-free power generation and refrigeration, and alleviate current

energy dilemma.[1-3] To evaluate efficiency of thermoelectric materials, the dimensionless figure of merit (zT) is defined as: $zT = S^2\sigma T/\kappa = S^2\sigma T/(\kappa_e + \kappa_l)$, where S, σ, κ, κ_e, κ_l, and T are the Seebeck coefficient, electrical conductivity, total thermal conductivity, electrical thermal conductivity, lattice thermal conductivity, and the absolute temperature, respectively.[4-6] To achieve high zT, efforts have been devoted to improving the power factor ($S^2\sigma$) through doping engineering[7-9] or band structure engineering,[10-12] and reducing the κ_l through nanostructure engineering.[13-15]

Low-temperature thermoelectric materials are well-known for their high conversion efficiency around the room temperature,[16,17] and have especial attractions as the power source for wearable electronics.[5] Bismuth telluride (Bi_2Te_3), as one of the best low-temperature thermoelectric materials, has intrinsically decent electrical properties due to its narrow band gap (~0.15 eV) with high valley degeneracy and anisotropic effective mass.[18] By means of alloying/doping with elements,[19,20] its electrical performance can be further boosted, and a record-high $S^2\sigma$ of ~45 μW cm^{-1} K^{-2} was reported at 300 K from both S-doped Bi_2Te_3[20] and $Bi_{0.5}Sb_{1.5}Te_3$.[17] In order to further enhance its zT, various efforts have been devoted to reducing κ_l by inducing strong phonon scatterings.[16,17,21] Specifically, defect engineering, including the introduction of lattice defects, such as point defects[16] or dislocations,[17] was reported in the Bi_2Te_3-based alloys. With the effective phonon scatterings due to defect engineering, reduced κ_l of ~0.3 W m^{-1} K^{-1} was achieved at 300 K in the $Bi_{0.5}Sb_{1.5}Te_3$.[17] Moreover, nanostructure engineering was reported to induce a high density of grain boundaries in the Bi_2Te_3. As a result, significant phonon scatterings were found, leading to ultralow κ_l of ~0.2 W m^{-1} K^{-1} at 370 K.[21] In addition, porous structure is also known to effectively reduce κ_l.[22-24] Due to the intensive phonon scatterings at the pore-induced interfaces, ultralow κ_l of 0.13 W m^{-1} K^{-1} was reported at 488 K in the $Bi_2Te_{2.5}Se_{0.5}$.[24] In spite of these progresses, lower κ_l

is still desiring for Bi_2Te_3 to achieve higher zT. According to the Callaway model, κ_l has positive

relevance with the phonon relaxation time (τ), as defined below:[25]

$$\kappa_l = \frac{1}{3}\int_0^{\omega_{max}} C_s(\omega)v_g(\omega)^2\tau(\omega)d\omega \ , \tag{1}$$

where C_s is the spectral heat capacity and v_g is the phonon group velocity. Based on the Matthiessen

rule,[26] τ is negatively related to the sum effects of different phonon scattering sources. Therefore,

the combination of different phonon scattering sources can contribute to smaller τ due to full-

spectrum phonon scattering, which may in turn lead to lower κ_l.

Here, we prepared nanostructured n-type Bi_2Te_3 with porous structure via a facile solvothermal

method, and subsequent sintered them into pellets through the sparking plasma sintering (SPS), as

schematically shown in **Figure 1**. During the sintering process, the impurity Bi_2TeO_5 sublimed

under the heating environment and large plasma currents.[27] Consequently, nanostructured Bi_2Te_3

with porous structure was fabricated. With the synergistic effects of both pores and nanostructure,

strong phonon scatterings were induced, leading to ultralow κ_l < 0.1 W m^{-1} K^{-1} at 420 K.

Consequently, a promising zT of 0.97 was achieved at 420 K, which is among the highest values

reported for pure n-type Bi_2Te_3.[21,22,28,29]

EXPERIMENTAL SECTION

Synthesis Method

Bi_2Te_3 nanoplates were synthesized via a typical solvothermal route. Analytical grade bismuth

oxide (Bi_2O_3, 99.9%), tellurium dioxide (TeO_2, 99.999%), ethylene glycol (EG),

polyvinylpyrrolidone (PVP, average molecular weight = 40000) and sodium hydroxide (NaOH,

99.99%) were purchased from Sigma-Aldrich as precursors without any further purification.

During the synthesis, PVP was firstly dissolved into EG (36 ml) as the surfactant, followed by 20 min vigorous stirring in order to form a clear solution. Bi_2O_3 and TeO_2 were then added into the solution as the source materials of Bi and Te, respectively. 5 mol L^{-1} NaOH (4 ml) was dropped into the solution to provide the alkaline environment. The solution was stirred for 30 min to uniformly mix precursors, before sealed in a 125 ml polytetrafluoroethylene-lined stainless-steel autoclave. The autoclave was heated to 210 ^{0}C for 24 h and naturally cooled down to the room temperature. Synthesized products were collected by centrifugation and washed with deionized water and ethanol for several times, and finally dried in the oven at 60 ^{0}C for 12 h.

Spark Plasma Sintering and Thermoelectric Properties Measurements

In order to measure the thermoelectric properties, synthesized powders were sintered into a disc-shaped pellet (Φ = 12.6 mm) by SPS (SPS-211Lx, Fuji Electronic Co., Ltd.) at 300 ^{0}C for 5 min under 60 MPa pressure. Density (ρ) of the pellet (85%) was measured using the Archimedes method. Due to the intrinsic anisotropy of Bi_2Te_3,[30-32] thermoelectric properties of the pellets were measured in the in-plane direction, since it is the high-performance direction.[32] Among which, σ and S were measured simultaneously using ZEM3 (ULVAC Technologies, Inc.) within the temperature range between 300 and 573 K; the thermal diffusivity D was measured by LFA 457 (NETZSCH Group), which was subsequently applied to calculate $\kappa = D \cdot C_p \cdot \rho$,[33] where C_p is the specific heat capacity measured by DSC 404 C (NETZSCH Group); n and μ were measured by a Hall system under a reversible magnetic field of 1.5 T. All property measurements of the pellet were conducted for at least three times in order to ensure the repeatability.

Characterization

Both synthesized powder and sintered pellet were systematically characterized. X-ray diffraction (XRD, Bruker-D8) was applied to determine the composition and crystal structure of both as-synthesized Bi_2Te_3 powder and as-sintered Bi_2Te_3 pellet, where the pellet was characterized along the in-plane direction. X-ray spectroscopy (XPS) (Kratos Axis Ultra) was used to investigate the valence states of Te in Bi_2Te_3 and Bi_2TeO_5. Scanning Electron Microscopy (SEM, JEOL JSM-7100F) was utilized to observe the morphology and structural characteristics. Electron probe micro-analyzer (EPMA, JEOL JXA-8200) was used to determine the chemical composition of the pellet. The instrumental deviation of EPMA is 0.1% and ten randomly selected areas of the pellet were measured. Energy-dispersive X-ray spectroscopy (EDS) mapping and spot analysis (equipped in HITACHI-SU3500 SEM) were conducted to verify the element distribution and the chemical composition of the sample, respectively.

RESULTS AND DISCUSSION

Figure 2a shows the XRD patterns of as-synthesized Bi_2Te_3 powder and as-sintered Bi_2Te_3 pellet along the in-plane direction, respectively. Compared with standard Bi_2Te_3 diffraction pattern (PDF#15-0863), (0 0 15) diffraction peaks of both Bi_2Te_3 powder and pellet samples are found to shift towards higher degree, indicating the lattice shrinkage, as shown in Figure S1 (ESI†). The diffraction peaks of the powder can be exclusively indexed as the rhombohedral structured Bi_2Te_3 with the lattice parameters of a = 4.3852 nm, c = 30.483 nm and a space group of R$\overline{3}$m (PDF#15-0863), and orthorhombic structured Bi_2TeO_5 with the lattice parameters of a = 16.447 nm, b = 5.513 nm, c = 11.579 nm and a space group of Cm2a (PDF#38-0420). However, after the SPS process, diffraction peaks of as-sintered pellet can be only indexed as the rhombohedral structured

Bi_2Te_3. The disappearance of Bi_2TeO_5 during the sintering process should be attributed to the sublimation of Bi_2TeO_5 under SPS heat treatments and large currents.[27] The XPS was further utilized to verify the sublimation of Bi_2TeO_5 during the SPS process. The full XPS spectra of both Bi_2Te_3 nano-powder and nanostructured Bi_2Te_3 pellet (shown in Figure S2, ESI†) indicate the presences of Bi 4f and Te 3d energy states, without any energy states detected for other elements, except C 1s and O 1s. High-resolution scans of XPS spectra for Bi 4f show no obvious difference after the sintering, where peaks of Bi $4f_{5/2}$ and Bi $4f_{7/2}$ were found at 162.5 eV and 157.2 eV, respectively, as shown in Figure S2, ESI†. This implies the existence of single valence state Bi^{3+} in both Bi_2Te_3 nano-powder and porous nanostructured Bi_2Te_3 pellet.[37] **Figure 2**b and c show the high-resolution scans of XPS spectra for Te, in which strong singlet peaks of Te $3d_{5/2}$ and Te $3d_{3/2}$ were detected at the binding energy of 572.23 eV and 582.53 eV in both powder and pellet, respectively. This indicates the existence of Te^{2-}.[34,35] Additional peaks at the binding energy of 575.67 eV and 586.14 eV, evidencing the existence of Te^{4+}, were only found in the powders.[35] The Te^{2-} and Te^{4+} should be ascribed to Bi_2Te_3 and Bi_2TeO_5, respectively. The disappearance of Te^{4+} peaks after the SPS process further confirms the sublimation of Bi_2TeO_5.

Figure 3a-c show SEM images of as-synthesized Bi_2Te_3 powder. As can be seen, as-synthesized Bi_2Te_3 powders are consisted of hexagonal nanoplates, with a typical thickness of ~20 nm, as shown in the inset of Figure 3c. Such nanostructures can induce a high density of grain boundaries in the pellet after the sintering.[29] Figure 3d-3f show SEM images of as-sintered nanostructured Bi_2Te_3 pellet. As highlighted in the image, porous structure can be clearly seen, where pores homogeneously distribute in the matrix. Figure 3f shows a typical pore with a size of ~400 nm in the matrix.

Figure 4a show the EDS results obtained from as-sintered nanostructured porous Bi_2Te_3 pellet. EDS spot analysis (spot highlighted in the inset) suggests that the sample show binary composition, with Bi and Te exclusively detected. EDS mapping and corresponding backscattered electrons (BSE) SEM image are shown as the inset, where homogeneous distributions of Bi and Te were observed. The atomic ratios of Bi and Te were evaluated as 41.2 % and 58.8 %, respectively. Figure 4b shows the EPMA results, where the composition of as-sintered nanostructured porous pellet was more accurately determined. The average ratio between Bi and Te in the pellet is ∼ 0.715, indicating a composition of $Bi_2Te_{2.8}$. Such a Te vacancy is consistent with the observed lattice shrinkage in our XRD results. Detailed compositions of Bi and Te detected by EPMA can be found from Table S1 (ESI†) in the supporting information.

Figure 5 shows the measured thermoelectric properties of as-sintered nanostructured porous Bi_2Te_3 pellet along the in-plane direction, including σ, n, μ, S and κ. In order to understand the effects of porous structure, thermoelectric properties are compared with previously reported dense nanostructured Bi_2Te_3 pellet.[21] As shown in Figure 5a, σ shows no obvious difference than that of the dense nanostructured Bi_2Te_3 pellet, and decreased gradually with T, presenting typical metallic transport behaviours.[36] The peak σ of 770 S cm^{-1}, occurred at 300 K, is comparable to other reported pure Bi_2Te_3.[21,28,37] Figure 5b shows measured n and μ, in which n slightly increases from 7×10^{19} cm^{-3} to 1×10^{20} cm^{-3} in the temperature range of 300 to 550 K, while μ gradually decreases with T, with the value of 66 cm^2 V^{-1} s^{-1} at 300 K. Such a μ is similar to other porous Bi_2Te_3-based pellets.[24,38] In terms of S, as shown in Figure 5c, negative values were obtained, indicating typical n-type properties. The peak value of -145 µV K^{-1} was measured at ∼ 450 K, which is also similar to that of the dense nanostructured Bi_2Te_3.[21,37] As a result, Figure 5d shows uncompromised $S^2\sigma$ that has a peak value of 12.89 µW cm^{-1} K^{-2} at 320 K. It can be concluded that the introduction of

pores possesses negligible effects on electrical properties of our nanostructured porous Bi_2Te_3 pellet along the in-plane direction. This may be ascribed to the typical layered structure of Bi_2Te_3, where the carrier transport in the in-plane direction (*ab* direction) primarily contributes to the system carrier transport, compared with that in the out-of plane direction (*c* direction).[30-32] The pores observed here have limited influences on the atomic scale layered structure. Hence, the high carrier transport properties can be secured by nearly undisturbed layered structures.

Figure 6 shows calculated κ. The results of measured D and C_p from 300 K to 550 K can be found from Figure S3, ESI†. It was found that the introduction of pores leads to lower κ at all temperature range from 300 to 560 K, with the lowest value of ~0.5 W m^{-1} K^{-1} at 418 K. To understand such an ultralow κ, we investigated κ_e and κ_l using the Wiedemann – Franz law,[39] where $\kappa_e = L\sigma T$ and $\kappa_l = \kappa - \kappa_e$. L is the Lorenz number (~ 1.8×10^{-8} v^2 K^{-2}) and was calculated based on SPB model (Figure S3, ESI†).[40,41] It was found that κ_e lies in the range of 0.39 to 0.47 W m^{-1} K^{-1} (Figure S3, ESI†), which is comparable to the values of dense nanostructured Bi_2Te_3.[21] Therefore, the reduction of κ of the as-sintered nanostructured porous Bi_2Te_3 pellet mainly derives from κ_l. Figure 6a shows calculated κ_l in as-sintered porous nanostructured Bi_2Te_3 pellet. It was found porous structure can effectively reduce κ_l and ultralow κ_l of <0.1 W m^{-1} K^{-1} was found at 370 K. This significant κ_l reduction can be explained by the phonon gas theory, where κ_l can be written as $\kappa_l = (1/3)C_v v l$. Among which, C_v is the specific heat capacity at a constant volume, v is the sound velocity, and l is the phonon mean free path.[42] Reduced ρ of the porous pellet can negatively contribute to C_v, considering $C_v = C'_v \rho$, where C'_v reflects the specific heat properties of the materials.[43] Moreover, formation of pores has been proved to reduce v and l of thermoelectric materials.[43] As a result, κ_l was significantly reduced in our porous structure, and in turn lead to ultralow κ.[44-51] Benefited from uncompromised $S^2\sigma$ and effectively reduced κ, we ultimately

realized boosted zT near 1 at 370 K, as shown in the Figure 6b. Such a promising zT is among the highest values reported for pure n-type Bi_2Te_3 so far, as shown in Figure S4 (ESI†).[21,28,29] Figure 6c compared our results with previously reported porous[22] or nanostructured Bi_2Te_3,[21] it was found that the simultaneous introduction of the nanostructure and the porous structure in our study can effectively generate further reduced κ_l, which in turn produce improved zT. Based on the analysis of single parabolic band (SPB) model as shown in Figure 6d,[40,41] further reduced κ_l could potentially pushes zT to a higher level with appropriately engineered n_e (Section 5 in the Supporting Information shows detailed calculations). The higher n_e than predicted optimal value in our work may be associated with the high level of Te vacancy. Further control of Te vacancy might be of interest in our future study to effectively reduce n_e and in turn achieve higher zT.

CONCLUSIONS

In summary, we fabricated n-type porous nanostructured Bi_2Te_3 pellet with facile solvothermal method and subsequent SPS. With adequate sublimations of Bi_2TeO_5 during the sintering process, homogeneously distributed pores were successfully introduced into the nanostructured Bi_2Te_3 pellet. As a consequence of simultaneous strong phonon scatterings at both dense grain boundaries of nanostructure and interfaces induced by pores, an ultralow κ_l (< 0.1 W m^{-1} K^{-1}) was realized. The well-maintained decent electrical performance, a $S^2\sigma$ of 10.57 µW cm^{-1} K^{-2} at 420 K, as well as the reduced κ_l secured a promising zT of 0.97, which is among the highest values reported for pure n-type Bi_2Te_3.[21,22,28,29] This study provides an alternative insight of realizing ultralow κ_l by synergistic phonon scatterings induced by pores and nanostructure in n-type Bi_2Te_3-based thermoelectric materials.

1
2
3
4
5
6
7
8
9
10
11
12
13
14
15
16
17
18
19
20
21
22
23
24
25
26
27
28
29
30
31
32
33
34
35
36
37
38
39
40
41
42
43
44
45
46
47
48
49
50
51
52
53
54
55
56
57
58
59
60

ASSOCIATED CONTENT

Supporting Information. XPS spectra; Lorenz factor and measured thermal properties;

EPMA results; and SPB calculation details.

AUTHOR INFORMATION

Corresponding Author

*E-mail: zhigang.chen@usq.edu.au (Z-G. Chen)

zhigang.chen@uq.edu.au (Z-G. Chen)

ACKNOWLEDGMENTS

REFERENCES:

(1) Chen, Z.-G.; Han, G.; Yang, L.; Cheng, L.; Zou, J. Nanostructured Thermoelectric Materials: Current Research and Future Challenge. *Prog. Nat. Sci.* **2012,** *22*, 535-549.

(2) Yang, L.; Chen, Z.-G.; Dargusch, M. S.; Zou, J. High Performance Thermoelectric Materials: Progress and Their Applications. *Adv. Energy Mater.* **2018,** *8*, 1701797.

(3) Snyder, G. J.; Toberer, E. S. Complex Thermoelectric Materials. *Nat. Mater.* **2008,** *7*, 105-114.

(4) Liu, W.-D.; Chen, Z.-G.; Zou, J. Eco-Friendly Higher Manganese Silicide Thermoelectric Materials: Progress and Future Challenges. *Adv. Energy Mater.* **2018,** *8*, 1800056.

(5) Wang, Y.; Yang, L.; Shi, X.-L.; Shi, X.; Chen, L.; S. Dargusch, M.; Zou, J.; Chen, Z.-G. Flexible Thermoelectric Materials and Generators: Challenges and Innovations. *Adv. Mater.* **2019,** *31*, 1807916.

(6) Shi, X.-L.; Zheng, K.; Liu, W.-D.; Wang, Y.; Yang, Y.-Z.; Chen, Z.-G.; Zou, J. Realizing High Thermoelectric Performance in *n*-Type Highly Distorted Sb-Doped SnSe Microplates *via* Tuning High Electron Concentration and Inducing Intensive Crystal Defects. *Adv. Energy Mater.* **2018,** *8*, 1800775.

(7) Moshwan, R.; Shi, X. L.; Liu, W. D.; Yang, L.; Wang, Y.; Hong, M.; Auchterlonie, G.;

Zou, J.; Chen, Z. G. High Thermoelectric Performance in Sintered Octahedron-Shaped

$Sn(CdIn)_xTe_{1+2x}$ Microcrystals. *ACS Appl. Mater. Interfaces* **2018,** *10*, 38944-38952.

(8) Hong, M.; Chen, Z. G.; Yang, L.; Zou, Y. C.; Dargusch, M. S.; Wang, H.; Zou, J.

Realizing *zT* of 2.3 in $Ge_{1-x-y}Sb_xIn_yTe$ *via* Reducing the Phase-Transition Temperature

and Introducing Resonant Energy Doping. *Adv. Mater.* **2018,** *30*, 1705942.

(9) Shi, X.; Zheng, K.; Hong, M.; Liu, W.; Moshwan, R.; Wang, Y.; Qu, X.; Chen, Z. G.;

Zou, J. Boosting the thermoelectric performance of *p*-type heavily Cu-doped

polycrystalline SnSe *via* inducing intensive crystal imperfections and defect phonon

scattering. *Chem. Sci.* **2018,** *9*, 7376-7389.

(10) Hong, M.; Wang, Y.; Feng, T.; Sun, Q.; Xu, S.; Matsumura, S.; Pantelides, S. T.;

Zou, J.; Chen, Z. G. Strong Phonon-Phonon Interactions Securing Extraordinary

Thermoelectric $Ge_{1-x}Sb_xTe$ with Zn-Alloying-Induced Band Alignment. *J. Am. Chem.*

Soc. **2019,** *141*, 1742-1748.

(11) Pei, Y.; Shi, X.; LaLonde, A.; Wang, H.; Chen, L.; Snyder, G. J. Convergence of

electronic bands for high performance bulk thermoelectrics. *Nature* **2011,** *473*, 66-69.

(12) Fu, C.; Bai, S.; Liu, Y.; Tang, Y.; Chen, L.; Zhao, X.; Zhu, T. Realizing high figure of merit in heavy-band *p*-type half-Heusler thermoelectric materials. *Nat. Commun.* **2015,** *6*, 8144.

(13) Hong, M.; Wang, Y.; Liu, W.; Matsumura, S.; Wang, H.; Zou, J.; Chen, Z.-G. Arrays of Planar Vacancies in Superior Thermoelectric $Ge_{1-x-y}Cd_xBi_yTe$ with Band Convergence. *Adv. Energy Mater.* **2018,** *8*, 1801837.

(14) Hong, M.; Wang, Y.; Xu, S.; Shi, X.; Chen, L.; Zou, J.; Chen, Z.-G. Nanoscale pores plus precipitates rendering high-performance thermoelectric $SnTe_{1-x}Se_x$ with refined band structures. *Nano Energy* **2019,** *60*, 1-7.

(15) Li, M.; Cortie, D. L.; Liu, J.; Yu, D.; Islam, S. M. K. N.; Zhao, L.; Mitchell, D. R. G.; Mole, R. A.; Cortie, M. B.; Dou, S.; Wang, X. Ultra-high thermoelectric performance in graphene incorporated Cu_2Se: Role of mismatching phonon modes. *Nano Energy* **2018,** *53*, 993-1002.

(16) Hu, L.; Zhu, T.; Liu, X.; Zhao, X. Point Defect Engineering of High-Performance Bismuth-Telluride-Based Thermoelectric Materials. *Adv. Funct. Mater.* **2014,** *24*, 5211-5218.

(17) Kim, S. I.; Lee, K. H.; Mun, H. A.; Kim, H. S.; Hwang, S. W.; Roh, J. W.; Yang, D. J.; Shin, W. H.; Li, X. S.; Lee, Y. H.; Snyder, G. J.; Kim, S. W. Dense dislocation arrays embedded in grain boundaries for high-performance bulk thermoelectrics. *Science* **2015,** *348*, 109-114.

(18) Mishra, S. K.; Satpathy, S.; Jepsen, O. Electronic Structure and Thermoelectric Properties of Bismuth Telluride and Bismuth Selenide. *J. Phys. Condens. Matter* **1997,** *9*, 461-470.

(19) Liu, W.-S.; Zhang, Q.; Lan, Y.; Chen, S.; Yan, X.; Zhang, Q.; Wang, H.; Wang, D.; Chen, G.; Ren, Z. Thermoelectric Property Studies on Cu-Doped *n*-type $Cu_xBi_2Te_{2.7}Se_{0.3}$ Nanocomposites. *Adv. Energy Mater.* **2011,** *1*, 577-587.

(20) Mehta, R. J.; Zhang, Y.; Karthik, C.; Singh, B.; Siegel, R. W.; Borca-Tasciuc, T.; Ramanath, G. A new class of doped nanobulk high-figure-of-merit thermoelectrics by scalable bottom-up assembly. *Nat. Mater.* **2012,** *11*, 233-240.

(21) Yang, L.; Chen, Z. G.; Hong, M.; Han, G.; Zou, J. Enhanced Thermoelectric Performance of Nanostructured Bi_2Te_3 through Significant Phonon Scattering. *ACS Appl. Mater. Interfaces* **2015,** *7*, 23694-23699.

(22) Zhang, Y.; Day, T.; Snedaker, M. L.; Wang, H.; Kramer, S.; Birkel, C. S.; Ji, X.; Liu, D.; Snyder, G. J.; Stucky, G. D. A mesoporous anisotropic n-type Bi_2Te_3 monolith with low thermal conductivity as an efficient thermoelectric material. *Adv. Mater.* **2012,** *24*, 5065-5070.

(23) Zhang, Y.; Mehta, R. J.; Belley, M.; Han, L.; Ramanath, G.; Borca-Tasciuc, T. Lattice thermal conductivity diminution and high thermoelectric power factor retention in nanoporous macroassemblies of sulfur-doped bismuth telluride nanocrystals. *Appl. Phys. Lett.* **2012,** *100*, 193113.

(24) Xu, B.; Feng, T.; Agne, M. T.; Zhou, L.; Ruan, X.; Snyder, G. J.; Wu, Y. Highly Porous Thermoelectric Nanocomposites with Low Thermal Conductivity and High Figure of Merit from Large-Scale Solution-Synthesized $Bi_2Te_{2.5}Se_{0.5}$ Hollow Nanostructures. *Angew. Chem. Int. Ed. Engl.* **2017,** *56*, 3546-3551.

(25) Toberer, E. S.; Zevalkink, A.; Snyder, G. J. Phonon Engineering through Crystal Chemistry. *J. Mater. Chem.* **2011,** *21*, 15843.

(26) Hong, M.; Chen, Z. G.; Yang, L.; Zou, J. $Bi_xSb_{2-x}Te_3$ Nanoplates with Enhanced Thermoelectric Performance due to Sufficiently Decoupled Electronic Transport

Properties and Strong Wide-Frequency Phonon Scatterings. *Nano Energy* **2016,** *20*, 144-155.

(27) K.V.Domoratsky; E.F.Dudnik; V.F.Katkov; L.Ya.Sadovskaya. X-ray Investigations of Phase Transition in Bi_2TeO_5 Single Crystals. *Condens. Matter Phys.* **1999,** *2*, 591-594.

(28) Scheele, M.; Oeschler, N.; Meier, K.; Kornowski, A.; Klinke, C.; Weller, H. Synthesis and Thermoelectric Characterization of Bi_2Te_3 Nanoparticles. *Adv. Funct. Mater* **2009,** *19*, 3476-3483.

(29) Son, J. S.; Choi, M. K.; Han, M. K.; Park, K.; Kim, J. Y.; Lim, S. J.; Oh, M.; Kuk, Y.; Park, C.; Kim, S. J.; Hyeon, T. *n*-Type Nanostructured Thermoelectric Materials Prepared from Chemically Synthesized Ultrathin Bi_2Te_3 Nanoplates. *Nano Lett.* **2012,** *12*, 640-647.

(30) Yan, X.; Poudel, B.; Ma, Y.; Liu, W. S.; Joshi, G.; Wang, H.; Lan, Y.; Wang, D.; Chen, G.; Ren, Z. F. Experimental studies on anisotropic thermoelectric properties and structures of *n*-type $Bi_2Te_{2.7}Se_{0.3}$. *Nano Lett.* **2010,** *10*, 3373-3378.

(31) Fang, H.; Bahk, J.-H.; Feng, T.; Cheng, Z.; Mohammed, A. M. S.; Wang, X.; Ruan, X.; Shakouri, A.; Wu, Y. Thermoelectric Properties of Solution-Synthesized *n*-Type Bi_2Te_3

Nanocomposites Modulated by Se: An Experimental and Theoretical Study. *Nano Res.* **2015,** *9,* 117-127.

(32) Wang, M.; Tang, Z.; Zhu, T.; Zhao, X. The Effect of Texture Degree on the Anisotropic Thermoelectric Properties of $(Bi,Sb)_2(Te,Se)_3$ based Solid Solutions. *RSC Adv.* **2016,** *6,* 98646-98651.

(33) Liu, W.-D.; Shi, X.-L.; Gao, H.; Moshwan, R.; Xu, S.-D.; Wang, Y.; Yang, L.; Chen, Z.-G.; Zou, J. Kinetic Condition Driven Phase and Vacancy Enhancing Thermoelectric Performance of Low-Cost and Eco-Friendly $Cu_{2-x}S$. *J. Mater. Chem. C* **2019,** *7,* 5366-5373.

(34) Hoefer, K.; Becker, C.; Rata, D.; Swanson, J.; Thalmeier, P.; Tjeng, L. H. Intrinsic Conduction through Topological Surface States of Insulating Bi_2Te_3 Epitaxial Thin Films. *Proc. Natl. Acad. Sci. U S A* **2014,** *111,* 14979-14984.

(35) Fu, J.; Song, S.; Zhang, X.; Cao, F.; Zhou, L.; Li, X.; Zhang, H. Bi_2Te_3 Nanoplates and Nanoflowers: Synthesized by Hydrothermal Process and their Enhanced Thermoelectric Properties. *CrystEngComm* **2012,** *14,* 2159-2165.

(36) Song, E.; Baranovskiy, A.; Xu, E.; Busani, T.; Swartzentruber, B.; Zhang, S.; Amouyal, Y.; Martinez, J. A. Manipulating Thermal and Electronic Transports in Thermoelectric Bi_2Te_3 Nanowires by Porphyrin Adsorption. *AIP ADV.* **2018,** *8*, 105010.

(37) Tang, X.; Xie, W.; Li, H.; Zhao, W.; Zhang, Q. Preparation and Thermoelectric Transport Properties of High-Performance *p*-Type Bi_2Te_3 with Layered Nanostructure. *Appl. Phys. Lett.* **2007,** *90*, 012102.

(38) Mei, D.; Wang, H.; Li, Y.; Yao, Z.; Zhu, T. Microstructure and thermoelectric properties of porous $Bi_2Te_{2.85}Se_{0.15}$ bulk materials fabricated by semisolid powder processing. *J. Mater. Res.* **2015,** *30*, 2585-2592.

(39) Kim, H.-S.; Gibbs, Z. M.; Tang, Y.; Wang, H.; Snyder, G. J. Characterization of Lorenz Number with Seebeck Coefficient Measurement. *APL Mater.* **2015,** *3*, 041506.

(40) She, X.; Su, X.; Du, H.; Liang, T.; Zheng, G.; Yan, Y.; Akram, R.; Uher, C.; Tang, X. High thermoelectric performance of higher manganese silicides prepared by ultra-fast thermal explosion. *J. Mater. Chem. C* **2015,** *3*, 12116-12122.

(41) Xu, Y.; Li, W.; Wang, C.; Li, J.; Chen, Z.; Lin, S.; Chen, Y.; Pei, Y. Performance optimization and single parabolic band behavior of thermoelectric MnTe. *J. Mater. Chem. A* **2017,** *5,* 19143-19150.

(42) Slack, G. A.; Ross, R. G. Thermal Conductivity under Pressure and through Phase Transitions in Solid Alkali Halides. II. Theory. *J. Phys. C: Solid State Phys.* **1985,** *18,* 3957-3980.

(43) Zhao, K.; Duan, H.; Raghavendra, N.; Qiu, P.; Zeng, Y.; Zhang, W.; Yang, J.; Shi, X.; Chen, L. Solid-State Explosive Reaction for Nanoporous Bulk Thermoelectric Materials. *Adv. Mater.* **2017,** *29,* 1701148.

(44) Liu, Y.; Zhao, L.-D.; Zhu, Y.; Liu, Y.; Li, F.; Yu, M.; Liu, D.-B.; Xu, W.; Lin, Y.-H.; Nan, C.-W. Synergistically Optimizing Electrical and Thermal Transport Properties of BiCuSeO *via* a Dual-Doping Approach. *Adv. Energy Mater.* **2016,** *6,* 1502423.

(45) Ge, Z. H.; Song, D.; Chong, X.; Zheng, F.; Jin, L.; Qian, X.; Zheng, L.; Dunin-Borkowski, R. E.; Qin, P.; Feng, J.; Zhao, L. D. Boosting the Thermoelectric Performance of (Na,K)-Codoped Polycrystalline SnSe by Synergistic Tailoring of the Band Structure and Atomic-Scale Defect Phonon Scattering. *J. Am. Chem. Soc.* **2017,** *139*, 9714-9720.

(46) Xiao, Y.; Wu, H.; Li, W.; Yin, M.; Pei, Y.; Zhang, Y.; Fu, L.; Chen, Y.; Pennycook, S. J.; Huang, L.; He, J.; Zhao, L. D. Remarkable Roles of Cu to Synergistically Optimize Phonon and Carrier Transport in *n*-Type PbTe-Cu_2Te. *J. Am. Chem. Soc.* **2017,** *139*, 18732-18738.

(47) Xiao, Y.; Chang, C.; Pei, Y.; Wu, D.; Peng, K.; Zhou, X.; Gong, S.; He, J.; Zhang, Y.; Zeng, Z.; Zhao, L.-D. Origin of low thermal conductivity in SnSe. *Phys. Rev. B.* **2016,** *94*.

(48) Chen, Z.-G.; Shi, X.; Zhao, L.-D.; Zou, J. High-performance SnSe thermoelectric materials: Progress and future challenge. *Prog. Mater. Sci.* **2018,** *97*, 283-346.

(49) Chang, C.; Tan, Q.; Pei, Y.; Xiao, Y.; Zhang, X.; Chen, Y.-X.; Zheng, L.; Gong, S.; Li, J.-F.; He, J.; Zhao, L.-D. Raising thermoelectric performance of *n*-type SnSe *via* Br doping and Pb alloying. *RSC Adv.* **2016,** *6*, 98216-98220.

(50) Hong, M.; Chasapis, T. C.; Chen, Z. G.; Yang, L.; Kanatzidis, M. G.; Snyder, G. J.; Zou, J. *n*-Type $Bi_2Te_{3-x}Se_x$ Nanoplates with Enhanced Thermoelectric Efficiency Driven by Wide-Frequency Phonon Scatterings and Synergistic Carrier Scatterings. *ACS Nano* **2016,** *10*, 4719-4727.

(51) Moshwan, R.; Yang, L.; Zou, J.; Chen, Z.-G. Eco-Friendly SnTe Thermoelectric Materials: Progress and Future Challenges. *Adv. Funct. Mater.* **2017,** *27*, 1703278.
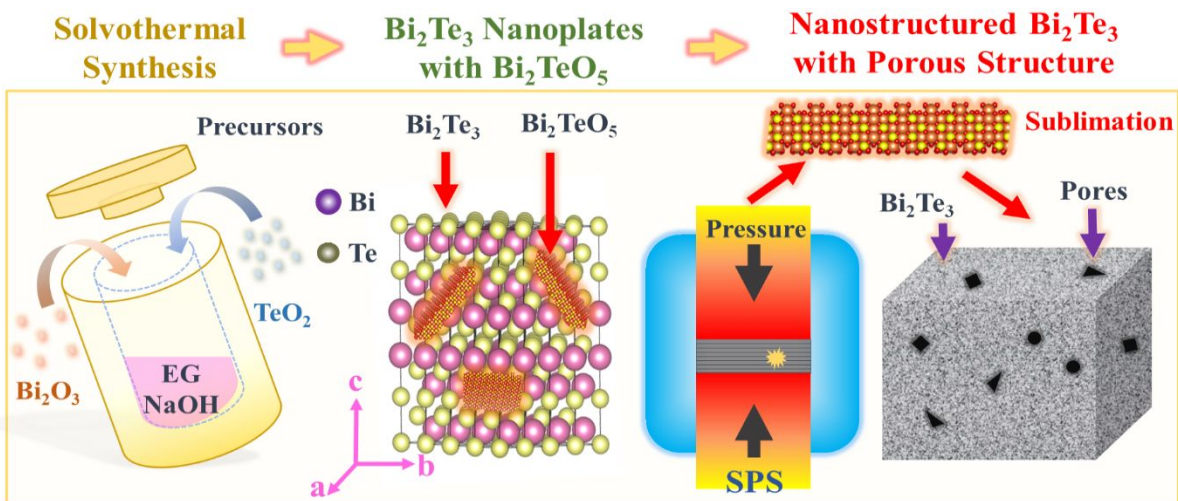
Figure 1. Illustration of the fabrication processes, where solvothermal synthesis and spark

plasma sintering were applied to fabricate porous nanostructured Bi_2Te_3 pellet.
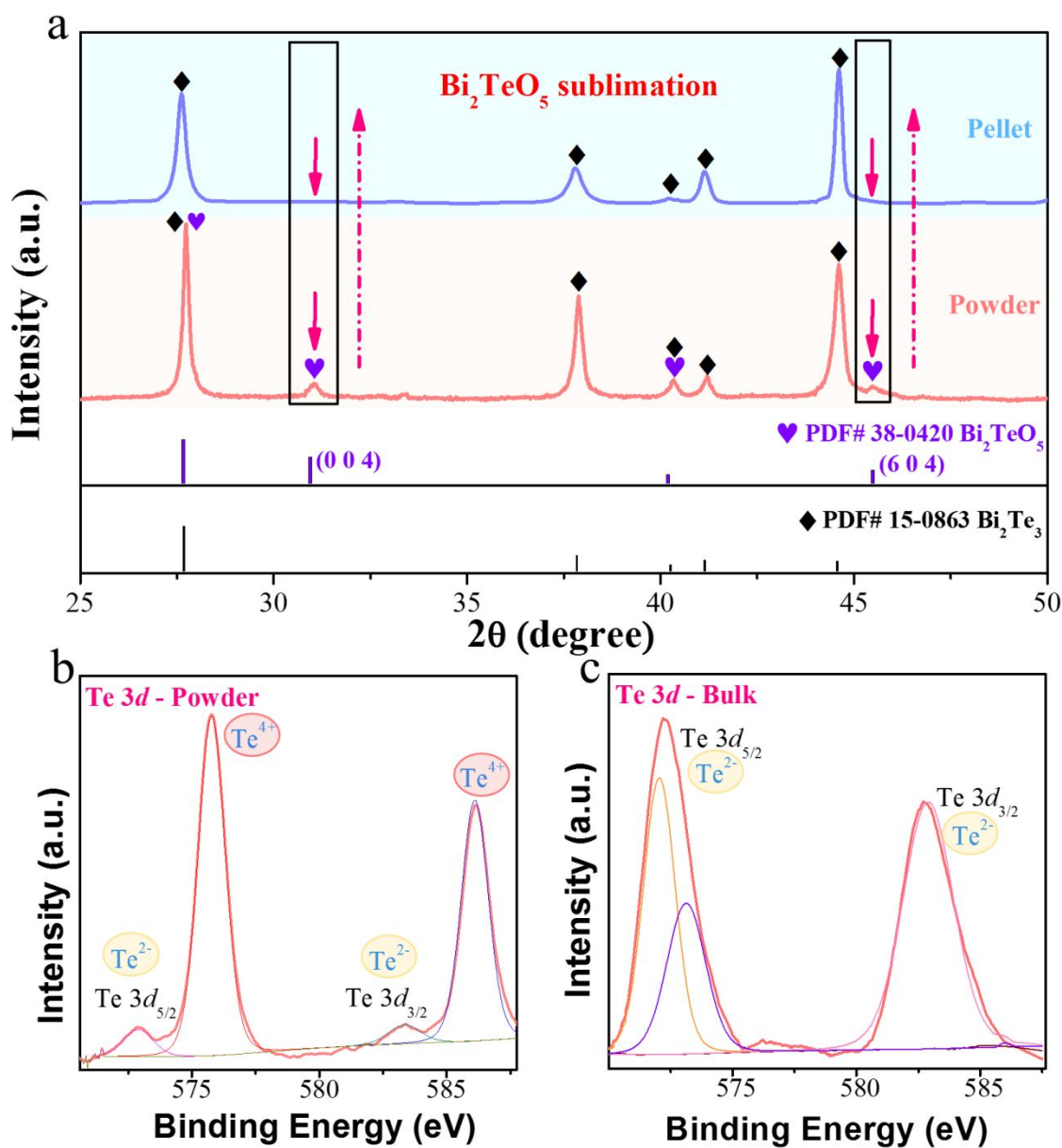
Figure 2. (a) XRD patterns of both as-synthesized Bi_2Te_3 nano-powders and as-sintered porous nanostructured Bi_2Te_3 pellet. High-resolution XPS scan of Te in the (b) as-synthesized Bi_2Te_3 nano-powder and (c) as-sintered porous nanostructured Bi_2Te_3 pellet.
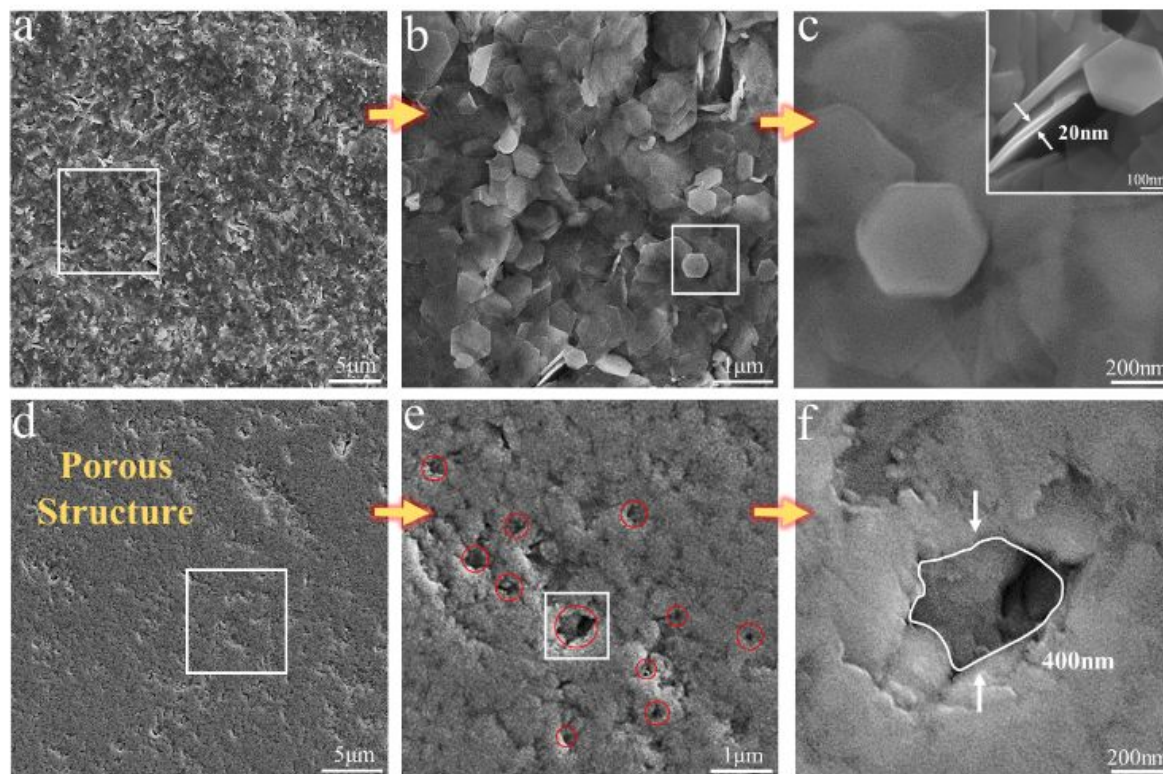
Figure 3. (a) SEM image of as-synthesized Bi_2Te_3 nano-powder; (b) magnified SEM

image of the area selected in (a); and (c) magnified SEM image of the area selected in

(b), showing the hexagonal plate-like nanostructure. Inset is the SEM image showing the

typical lateral thickness of the nanoplates is around 20 nm. (d) SEM image of as-sintered

nanostructured porous Bi_2Te_3; (e) magnified SEM image of the area selected in (d); and

(f) magnified SEM image of the pore selected in (e), showing the typical pore size of 400

nm.
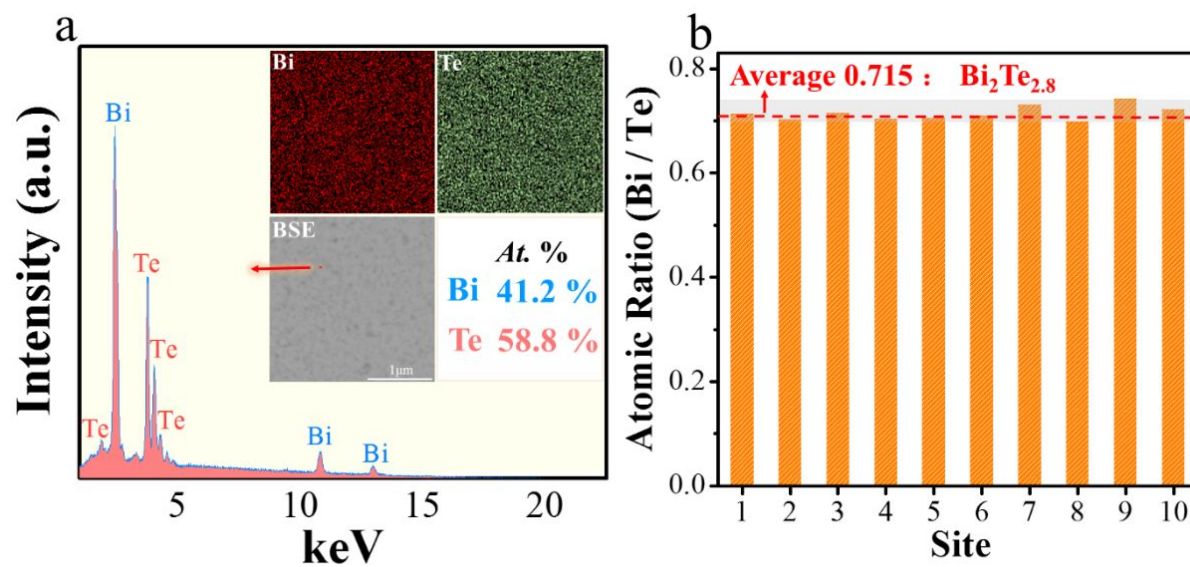
Figure 4. (a) EDS spot spectrum of as-sintered nanostructured porous Bi_2Te_3 pellet with

the inset of mapping results of Bi and Te. (b) Atomic ratios between Bi and Te measured

by EPMA at ten randomly selected area in the as-sintered nanostructured porous Bi_2Te_3
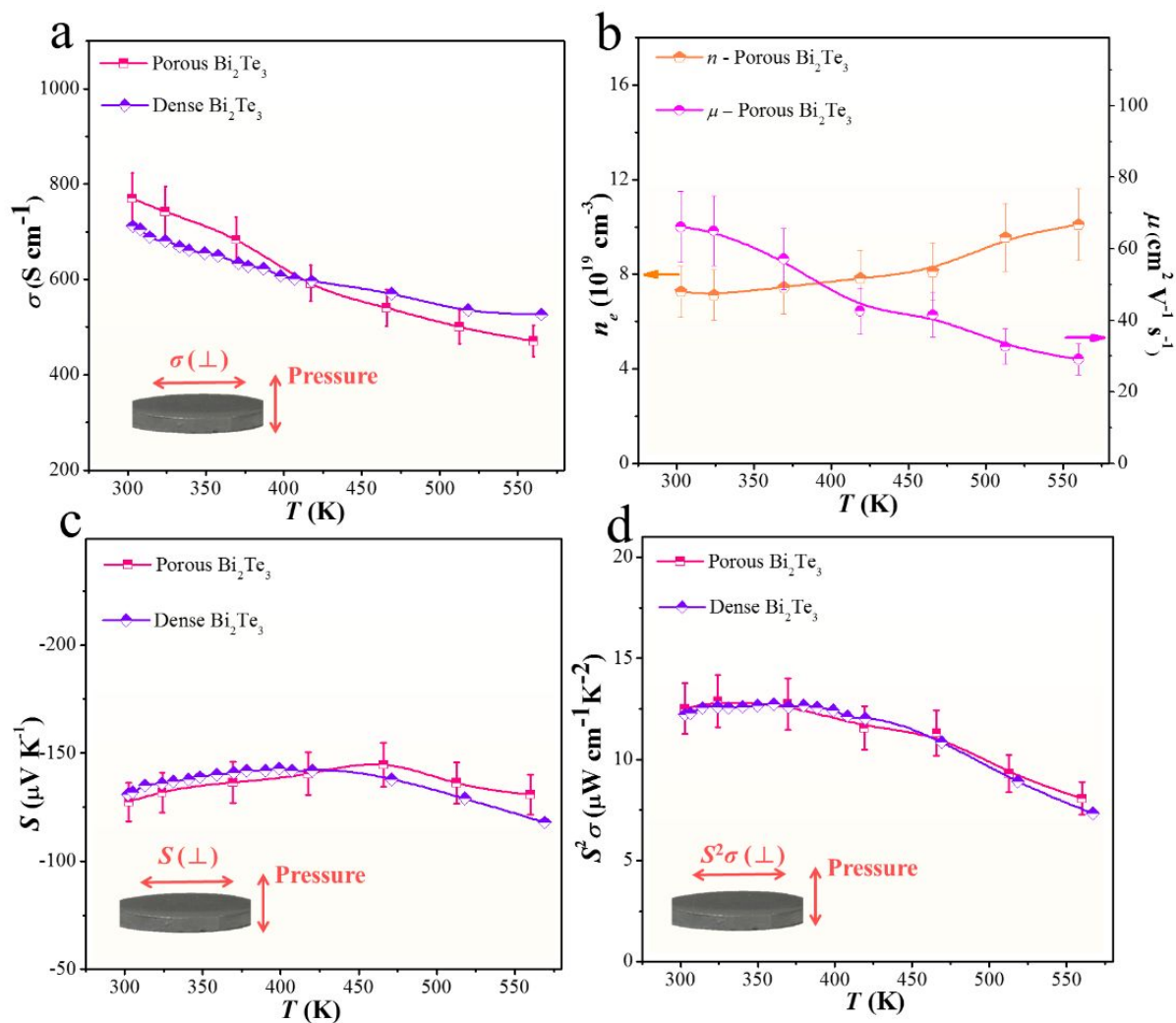
pellet.

Figure 5. T-dependent (a) σ; (b) n and μ; (c) S and (d) $S^2\sigma$ of as-sintered nanostructured

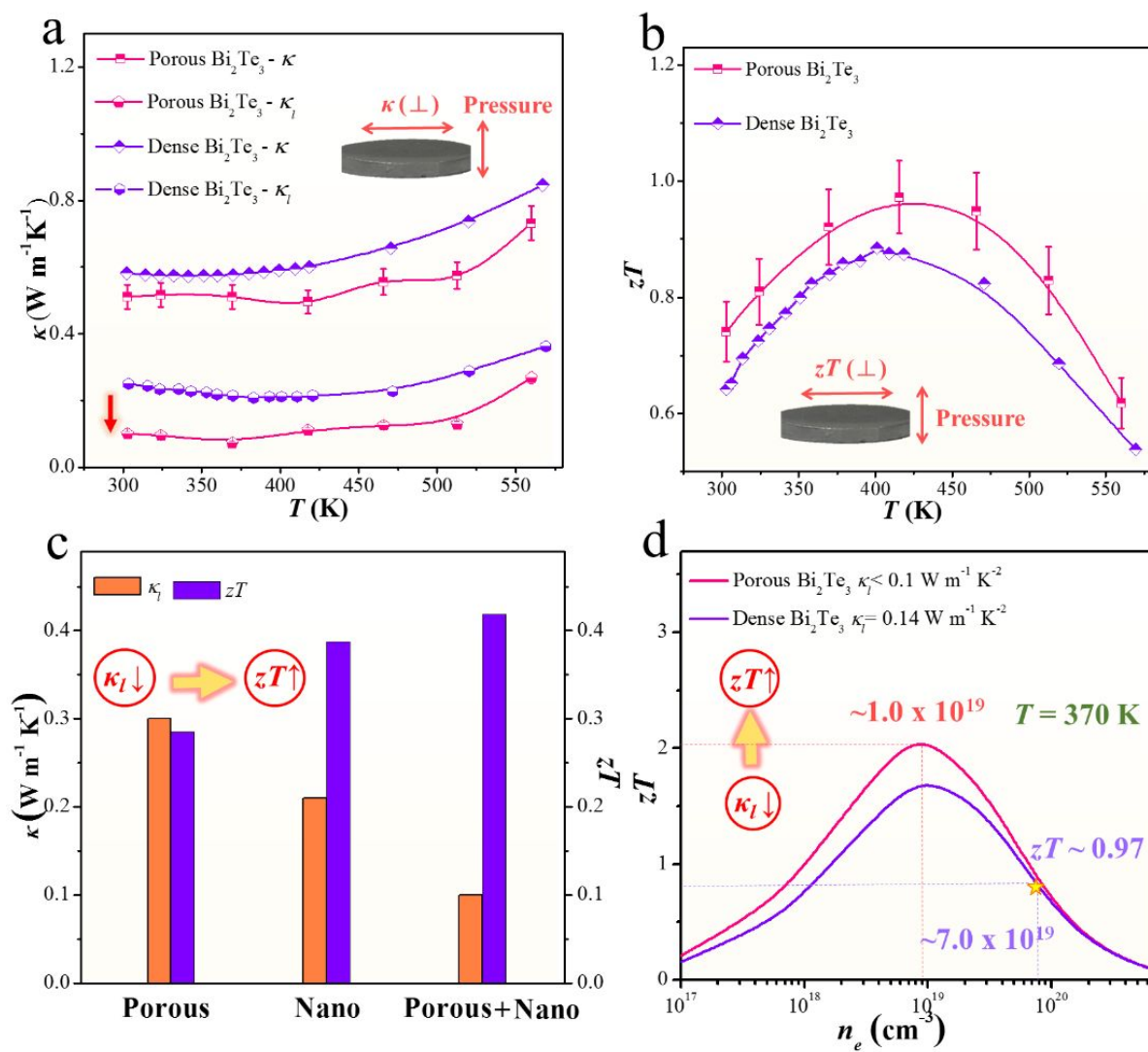porous Bi_2Te_3 pellet compared with dense nanostructured Bi_2Te_3.[9]

Figure 6. T-dependent (a) κ and κ_l; and (b) zT of as-sintered nanostructured porous Bi$_2$Te$_3$

pellet compared with dense nanostructured Bi$_2$Te$_3$.[9] (c) Comparisons of κ_l and zT

between this work and previously reported porous[10a] or nanostructured Bi_2Te_3.[9] (d)

Calculation results of SPB showing the possibility to further enhance zT with controlled

n_e and reduced κ_l.

Porous nanostructured Bi$_2$Te$_3$

TOC:

1
2
3
4
5
6
7
8
9
10
11
12
13
14
15
16
17
18
19
20
21
22
23
24
25
26
27
28
29
30
31
32
33
34
35
36
37
38
39
40
41
42
43
44
45
46
47
48
49
50
51
52
53
54
55
56
57
58
59
60

31